Influence of internal defects on filament wound SiC/SiC composite tubes on their mechanical behavior under uniaxial tension

C Morel, E Baranger, J Lamon, J Braun, C Lorrette

Influence of internal defects on filament wound SiC/SiC composite tubes on their mechanical behavior under uniaxial tension

C. Morel[1,2], E. Baranger[2], J. Lamon[2], J. Braun[1], and C. Lorrette[1]

[1] *Université Paris-Saclay, CEA, Service de Recherches Métallurgiques Appliquées, 91191 Gif-sur-Yvette, France*
[2] *Université Paris-Saclay, CentraleSupélec, ENS Paris-Saclay, CNRS, LMPS Laboratoire de Mécanique, 4 avenue des sciences, 91190 Gif-sur-Yvette, France*

Abstract

SiC/SiC composites are resistant to high temperatures making them excellent candidates for aeronautical or nuclear applications. The paper examines the robustness of the mechanical behavior of SiC/SiC tubes for fuel cladding in pressurized light water reactors. For this purpose monotonous tensile tests with loading – unloading cycles are carried on a serie of SiC/SiC tubes having standard dimensions and structural characteristics. They were made by chemical vapor infiltration (CVI) of the matrix into a wound fiber preform. The loading direction was parallel to the tube axis, and the fibers were oriented to $\pm 45°$ with respect to the tube axis. The tensile behavior is analyzed regarding the tube as a unidirectional structure reinforced by the fiber preform. The tensile behavior exhibits the conventional non linear deformations investigated in earlier works on dog bone specimens of SiC/SiC composite. The contribution of debonded interfaces in the vicinity of matrix cracks was determined from the loading-unloading loops. Two families of tubes were differentiated from features of the stress-strain behavior. The specimens of the second family displayed a decreased elastic modulus, slower rate of shear damage and premature saturation of slippage at fiber/matrix interface cracks. Various causes including the presence of free Si in the SiC matrix, the presence of seal coating, differences in local dimensions, arrangement of constituents, porosity, and cracks were examined.

Keywords Ceramic-matrix composites (CMCs), Mechanical properties, Tube, Defects, Tensile cyclic tests

1 Introduction

Ceramic matrix composites (CMCs) and in particular SiC/SiC composites are attractive materials for high-temperature applications due to their stability up

to 1600 °C [1, 2]. These materials are studied in many fields, e.g., aeronautics for combustion chambers or turbines, nuclear fuel cladding, due to their excellent thermo-mechanical properties [3]. Specifically, SiC/SiC composites are promising candidates for the fuel cladding in pressurized water nuclear reactors because of their high-temperature strength and stability under irradiation [4, 5]. These materials could increase the safety of reactors, in particular in case of EATF (Enhanced Accident Tolerant Fuel) application, which aims at safety margins for the fuel cladding in the event of a loss of coolant accident (LOCA) [6]. On the contrary to Zirconium-based fuel cladding, SiC/SiC composites would be able to maintain their dimensions and integrity in extreme conditions, beyond 1500 °C under steam [7, 8]. The oxidation is also strongly reduced compared to Zr-based fuel cladding in LOCA [6]. To this end, SiC/SiC tubular composites are investigated in order to replace Zr-based cladding and respect LWR (Light Water Reactor) cladding criteria [9, 10, 11].

Industrial researchers rarely considered CMCs tubular structures except for nuclear applications. Thus, some tubular components for the aerospace industry are used as a sublayer in turbine blade cooling systems or in propulsion engine cooling systems [12, 13]. For nuclear applications, researchers have already investigated the mechanical behavior of SiC/SiC tubes under various loading conditions and for different fiber preform structures. For 2D braided composites, tensile tests have been performed for studying the impact of different braiding angles on crack propagation [14]. Hybrid architectures, consisting of two layers of 2D braiding combined with a filament wound layer, have also been the subject of extensive research at CEA (French Alternative Energies and Atomic Energy Commission). Bi-axial tests, both tension-torsion and tension-internal pressure [15], as well as in-situ tension-compression tests have enabled a better understanding of the damage mechanisms [2]. Cyclic tension tests have been performed to understand the effect of residual thermal stresses induced during the manufacturing process on the mechanical behavior [16]. A new generation of tubes reinforced by wound preform have been proposed in recent years by CEA. Such tubes make it possible to reduce porosity in the material, ie., approximatively to 7 % against 11 % in braided tubes [17, 18] with smoother external surfaces while exhibiting a mechanical behavior close to that of 2D braided structures [19]. The multi-axial behavior of composites was also characterized on such structures. For example, tensile-compression-torsion tests have been performed on SiC/SiC tubes to highlight the anisotropy induced by damage [20]. These various experimental studies show the diversity of the different existing SiC/SiC tube structures for which the mechanical behavior is satisfactorily described. However, the relationship between manufacturing process and mechanical behavior was less explored.

The literature has paid less attention to the influence of manufacturing on the mechanical behavior of composites tubes. The impact of fiber architecture [13, 15], grinding conditions [21, 22, 23], cutting using different processes, such as water jet cutting or laser cutting, [24] or even drilling [25] has already been examined on CMC. By contrast, quite no attention was paid to the impact of CVI on the mechanical behavior of SiC/SiC composite tubes. In particular, the

effect of the presence of free silicon (Si) in the matrix of some specimens needs to be investigated.

The tensile behavior of a CMC exhibits different steps: an initial step of elastic deformation, then damage by matrix cracking and progressive breakage of fibers, and finally the ultimate rupture [26, 27, 28, 29]. Damage modeling of the matrix requires considering the fiber/matrix slippage along the interphase cracks in the vicinity of matrix cracks. However, the works on fiber slippage focused only on loading in a fiber direction [30, 31]. In the case of tubes with fibers inclined to the loading direction, the plies are subjected to multi-axial tension-shear loading.

This paper investigates the effect of various defects on the tensile behavior of SiC/SiC tubes made via CVI. The term "defect" denotes flaws and imperfection including inclusions (like free Si in the matrix), pores, cracks, variability in dimensions of constituents.

2 Materials and method

2.1 CVI-SiC/SiC manufacturing process

The manufacturing process for CVI-SiC/SiC tubes involves several steps, as described on Figure 1. First, the fibrous preform is produced using third generation of SiC fibers deemed to be of nuclear grade. Hi-Nicalon type S fibers are used, because they lead to higher damage tolerance and mechanical strength than Tyranno SA3 fibers [1]. The fibrous preform consists of two layers, oriented at $\pm 45°$, to have a balanced structure, with the same behavior whatever the loading, made in tension or in internal pressure. In addition, a filament winding architecture is preferred to the 2D braided one to obtain a smoother surface finish [19].

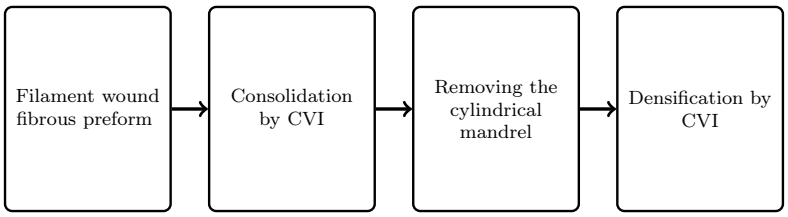

Figure 1: Different stages in the development of a CVI-SiC/SiC composite.

Two layers oriented at $\pm 45°$ have been wrapped around a cylindrical glass mandrel in filament winding. The winding parameters, including speed and fiber tension, have been carefully chosen to avoid fiber rupture during manufacturing [32].

The consolidation stage consists of the deposition of a pyrocarbon (30-100 nm) interphase and a few micrometers of silicon carbide matrix by CVI. At this stage, the fibrous preform is sufficiently rigid to remove the cylindrical

mandrel by chemical etching [32]. Then, the densification takes place until a SiC matrix volume fraction of around 60 %. Final porosity is less than 10 %. The average internal diameter is 8.27 mm, the average external diameter is 9.54 mm (average cross-section of $S \approx 17.58\,\mathrm{mm}^2$) close to the geometrey of standard LWR fuel cladding tubes. After CVI process, the surface roughness is high, respectively $R_a \approx 32\,\mu\mathrm{m}$ for external surface and $R_a \approx 11\,\mu\mathrm{m}$ for internal surface.

2.2 Description of the microstructure of CVI-SiC/SiC composite

Two first families of tubes were studied in this paper, identified as families 1-A and 1-B. For each family, the manufacturing process described above has been used. Family 1-A is the reference. In contrast, family 1-B contains a modification of the SiC matrix core related to the consolidation process during CVI. The tubes can be divided into two parts: the core ply containing matrix, fibers, and porosity, and the seal coat composed of matrix only. Sections at 90° to the tube axis at the top and the bottom of the sample were cut with a diamond wire saw and then cold coated and polish. These samples were observed under a digital microscope (VHX Keyance digital microscope with a VH-Z20R/W lens). As illustrated in Figure 2, surface fractions of fibers, matrix, and porosity obtained by digital microscopy are measured from cross-sectional images.

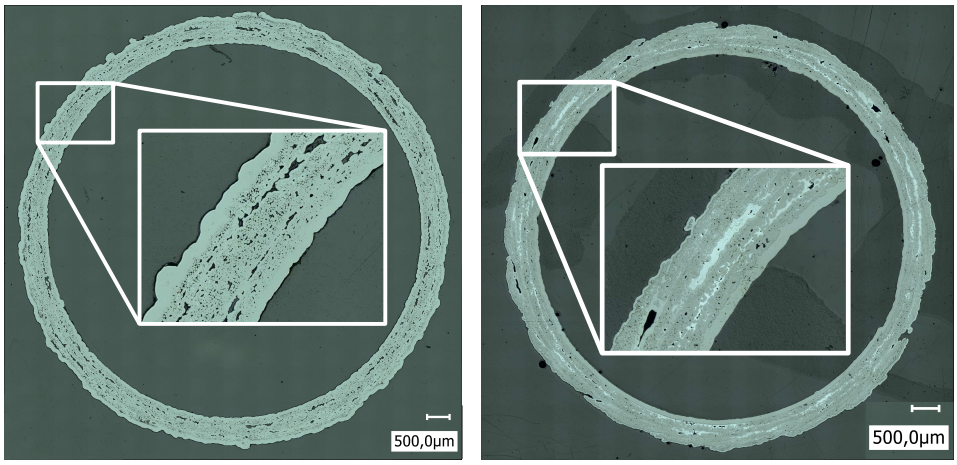

(a) 1-A (b) 1-B

Figure 2: Cross-sectional digital microscope images at ×400 magnification of (a) family 1-A and (b) family 1-B.

The tubes cross-section and porosity were measured on binarized cross section images. The histogram of the grey levels of the image was plotted for each of them to determine the optimal threshold level, as shown on Figure 3, where

the first peak correspond to the resin and the second one to the composite matrix and fiber. Therefore, the threshold value chosen corresponds to the bottom of the second peak, between 120 and 130 on the Figure 3 example. The cross-section is determined for five different threshold parameters both at the top and bottom of the tubes. The average of the two ends of the tube is the final section value kept for the stress determination. The porosity was determined by filling algorithms on the threshold images. This step was done for the different threshold parameters and images. The average of the two ends of the tube gives porosity rate.

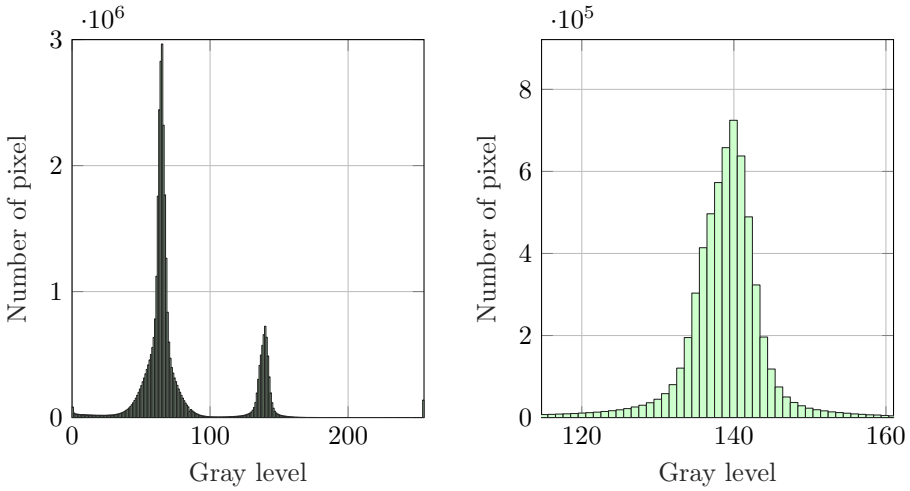

(a) Data over the whole range

(b) Zoom on the area of interest

Figure 3: Grey scale histogramm obtained on a cross-section image at 90° of the tube axis from family 1-A.

Regarding the determination of fiber content, the number of fibers were counted inside a part of the section to determine the representative value of the material. An average of five images that contain about 500 fibers each was done. The radius of the fibers was considered to be r_f =6.4 µm according [29] and the fibers were oriented at $\theta = \pm 45°$.

Two zones were differentiated in the microstructure: the seal coat and the core ply, as shown on Figure 4. The seal coat thicknesses on the outer and inner sides were measured. Six points of each section were taken and averaged. In order to determine the inner and outer radius of the tubes, the centers of the tubes were determined using the thresholded tube images. Fifty points were then selected on the inner and outer surfaces of the tube. The inner and outer radius of the tubes were then the average distance between the center and the selected points.

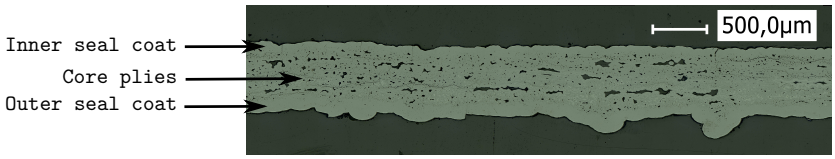

Figure 4: Digital microscopy of the manufactured SiC/SiC cross-section along its axis of revolution cut.

Eight tube samples were studied, three reference samples from family 1-A and five samples from family 1-B. The average characteristics for the two family are given in Table 1. The seal coat represents 19 % of the entire section, with a notable distinction between the distribution of the internal and external layers. The inner seal coat of 1-A is twice as thin as 1-B (52 µm for 1-A against 101 µm) while the external layer is larger in 1-A than 1-B (65 µm against 29 µm).

Family	1-A	1-B
Internal diameter	8.31 mm	8.22 mm
External diameter	9.59 mm	9.50 mm
Section	17.56 mm^2	17.60 mm^2
Internal seal coat thickness	52 µm	101 µm
Outer seal coat thickness	65 µm	29 µm
Percentage of seal coat	19 %	19 %

Table 1: Geometric characteristics for the families 1-A and 1-B.

Table 2 summerizes the composition data measured for the two families of tubes. The porosity mesured is relatively low for both families, less than 7 % of the whole section and 8 % of the core ply. Moreover, the porosity rate of family 1-B is 25 % lower than that of the reference family 1-A. The matrix fraction in 1-B is also higher, whereas elaboration of the fibrous preform was identical for both families.

Family	1-A	1-B
Porosity	6.3 %	4.6 %
Fiber	32.5 %	27.5 %
Matrix	61.2 %	67.9 %

Table 2: Composition of the families 1-A and 1-B: porosity, fibers and matrix contents.

Figure 5 shows representative backscattered electrons (BSE) images, putting into evidence the microstructure differences between both families of tubes. A high brightness can be interpreted as high nucleus charge (Z). The matrix is composed of silicon (Z =14) and carbon (Z =6), so the high brightness corresponds to pure silicon, which has a higher nucleus charge than SiC (14

for Si against 10 for the SiC, respectively). Figure 6 EDX mapping indicate a higher silicon concentration in 1-B compared to 1-A. In addition, the deposition rate of silicon is faster than the SiC deposition during the CVI process. Thus, 1-A has slightly higher porosity than 1-B.

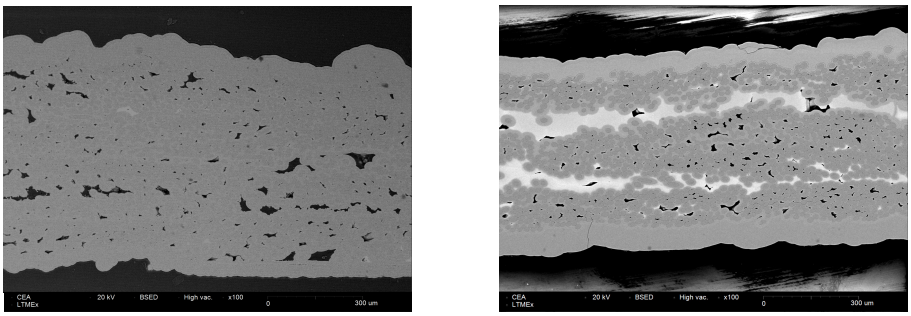

(a) 1-A (b) 1-B

Figure 5: BSE analysis representative of CVI-SiC/SiC for 1-A and 1-B. The white areas correspond to the presence of free Si in the inter-plies matrix.

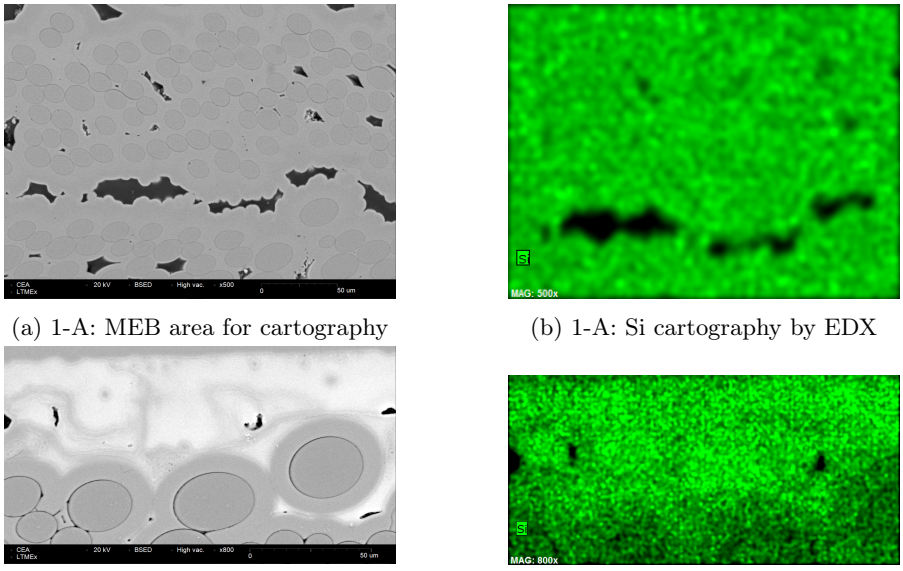

(a) 1-A: MEB area for cartography

(b) 1-A: Si cartography by EDX

(c) 1-B: MEB area for cartography

(d) 1-B: Si cartography by EDX

Figure 6: BSE observation on family 1-A and 1-B with the mapping of Si within the composite

In conclusion, several microstructural differences between the two families were observed, particularly the presence of Si in the core of the composite, the

porosity, and the thicknesses of the seal coat.

Another manufacturing batch was studied and two new families were prepared to separate the effect of the core and the seal coat on the mechanical behavior. The first family of this other manufacturing batch, labeled 2-RT (for raw CVI tube), allowed to study a tube whose outer and inner surfaces remained unmodified after the CVI process. The second series of tubes, labeled 2-WS (for without seal coat), enabled the analysis of a tube for which all seal-coat layers had been both externally and internally removed to investigate the core mechanical behavior. Table 3 shows the composition and geometry of 2-RT and 2-WS. These families are not the main focus of the study. Therefore, it allows understanding the influence of the seal coat and the core. The objective is to assess the analyses on 1-A and 1-B and the effect of the core modification.

	2-RT	2-WS
Number of samples	5	4
Inner diameter	8.31 mm	8.42 mm
Outer diameter	9.68 mm	9.32 mm
Inner seal coat thickness	58 µm	0 µm
Outer seal coat thickness	84 µm	0 µm
Percentage of fiber in the core	37 %	37 %
Percentage of porosity in the core	8.5 %	8.5 %

Table 3: Geometric characteristics of the families 2-RT and 2-WS of CVI-SiC/SiC tubes.

2.3 Mechanical test protocol

Uniaxial tensile tests in tube axis direction were carried out on 65 mm long tube samples. However, each ply was under combined tension and shear due to the local orientation of plies. The tests were performed according to ISO 20323 standard [33]. Tubes ends were bonded to collars using an epoxy adhesive glue (3M Scotch-Weld^{TM} 9323 B/A). This method ensured that the tubes were aligned with the direction of tension. The specimens were then mounted into the gripping system on the tensile machine (INSTRON 2404). The upper end collar was screwed on the upper grip, while the lower end collar was fixed with adhesive to the passive grip. The force measurements were performed with a 25 kN force cell (HBM U10M). The deformations were measured with a longitudinal extensometer class 0.5 (INSTRON 2620-603) of 25 mm gauge length ($\pm$1 mm course), and the displacement of the crossbar was controlled at a constant rate of 0.005 mm/min. An acoustic emission sensor (VS700-D by Vallen System) and a signal conditioner and data acquisition system (ASCO-DAQ2 by Vallen System) were used to determine the end of the elastic domain. The acoustic emission sensor was fixed on the upper end collar.

Both monotonic and cyclic tensile tests were performed to failure. The cycles were initiated at defined stress thresholds. Less than five cycles were carried out

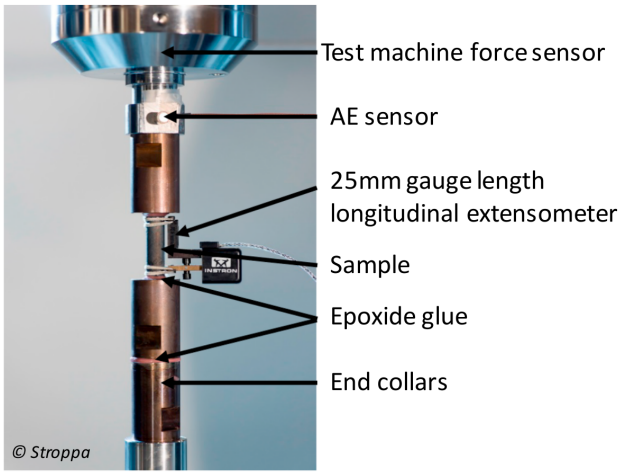

Figure 7: Tensile test experimental device (illustration extracted from [16]).

including the first cycle in the elastic domain. The samples were not subject to fatigue [16]. The unloading started at the stress thresholds of 50 MPa, 150 MPa, 200 MPa, 250 MPa and 300 MPa, to compression up to a stress of −50 MPa, to cause matrix cracks closure. Figure 8 shows the evolution of the strength as a function of time for two representative tests taken from 1-A and 1-B tubes. The plateau at 0 N corresponds to the compensation of the gap in the worm screw of the tensile machine. One monotonic tensile test and two cyclic tensile tests were performed on 1-A tubes; four monotonic tensile tests and one cyclic tests on 1-B tubes.

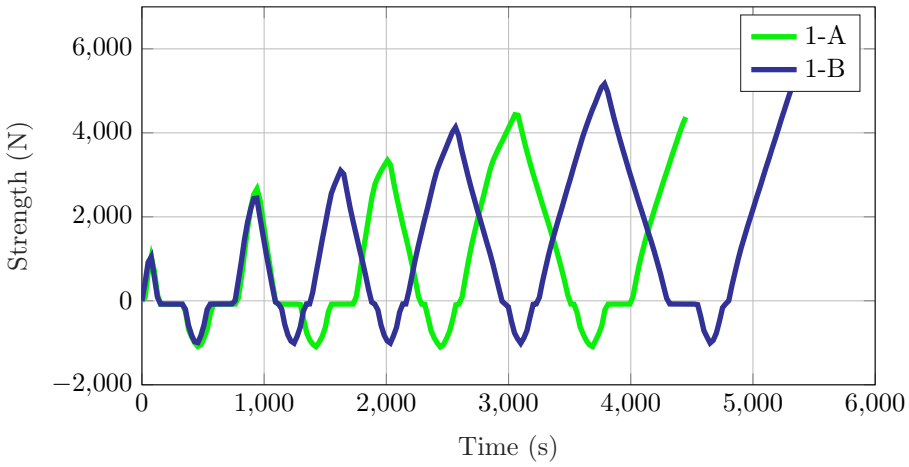

Figure 8: Evolution of the strength as a function of time for each family.

3 Elastic behavior of SiC/SiC tube

3.1 Elastic modulus

In the case of monotonic tests, the elastic modulus E_e was calculated by linear regression method between 0 MPa and 50 MPa. For the cyclic tensile tests, the elastic modulus was calculated by a linear regression method on the first cycle (from 0 MPa to 50 MPa with the return to compression at −50 MPa). The elastic cycle was carried out between 50 MPa and −50 MPa, the absence of acoustic emission confirms that there is no cracks on this stress range.

Figure 9 presents the elastic modulus for each sample from 1-A and 1-B. 1-A has an average modulus of 270 GPa, with a standard deviation of 3 GPa, against 212 GPa for 1-B, with a standard deviation of 9 GPa. Therefore, a 22 % decrease is observed on Si-containing samples.

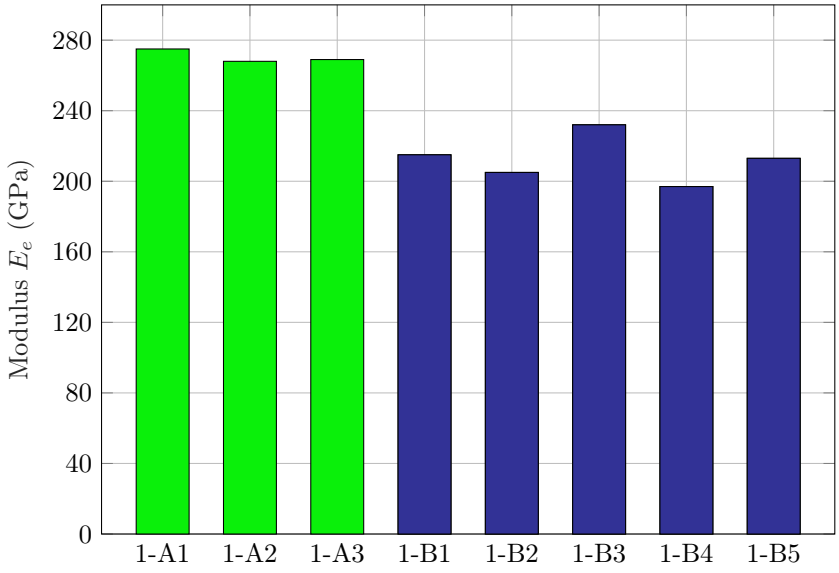

Figure 9: Elastic tangent moduli E_e for the two production families 1-A (green) and 1-B (blue).

However, several errors can influence the measured modulus. The sources of error can come from the strain which is measured with an extensometer. The class of the extensometer was 0.5, including a a relative error of 0.3 % for the strain measurement. The stress measurement is carried out with a load cell, and no error is considered on this measurement. The error on the stress comes mainly from the section measurement for which the repeatability error is evaluated at 4.9 %. Thus, the error on the elastic modulus is 5 % (i.e., ±14 GPa for 1-A and ±11 GPa for 1-B), far below the differences observed between the two families.

An analytical model based on continuum mechanics was proposed to precisely understand the influence of the volume fraction of each constituent on the elastic behavior. Geometrical considerations in this model assume a tube with different plies : two core plies oriented at $\pm 45°$ for the core of the material, and two plies inside and outside for the seal coat (Figure 10).

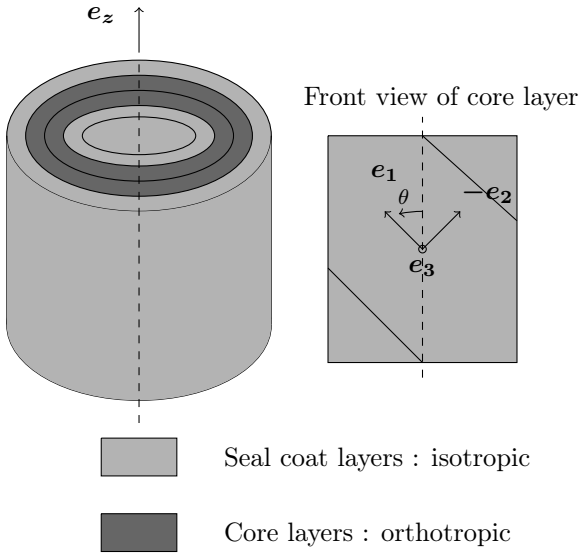

Figure 10: Theoretical geometry for the modeling of a tube composed of four layers: two for the core of the material, and two plies inside and outside for the seal coat.

The model respects the assumption of small perturbations and equilibrium. It also determines a behavior law for each ply. The two seal coat plies are composed only of the matrix; their mechanical behavior is considered to be isotropic. The numerical values are taken from Buet et al. [1] and given in Table 4. Internal plies require to consider the presence of porosity and fibers in addition to the matrix. The tensor of mechanical behavior is calculated at the base of the plies, oriented at 45°. Three steps are needed to build the constitutive law of the core. The matrix is first considered as an isotropic material; the porosity is then added in both fibers and transverse directions by making an analogy with the mesocraking behavior [34]. This model allows to take into account the orientation and the anisotropy of the porosity. In the last step, the fibers' behavior is added to the behavior of the internal plies by modifying only the elastic modulus in the fiber direction.

Quantity	Value
E_f	374 GPa
ν_f	0.19
E_m with SiC only	416 GPa
ν_m	0.19

Table 4: Main quantity and numerical value needed for the analytical elastic model (date from Buet et al. [1]).

The analytical model results can be compared with experimental Young's moduli measurements. For 1-A, a 260 GPa Young's modulus was calculated with the model, in comparison with the 273 GPa for the experimental value (Tables 1 and 2). The relative error is 4 %, which is lower than the modulus and geometry measurement errors.

Analytically determining the Young's modulus for the second family 1-B is challenging because the Si content in the core of the composite could not be precisely measured with accurency. The color contrasts between Si and SiC did not allow tracing the Si content by image analysis on the microscope images. An in-plane approximation of the Si fraction in the matrix is determined from BSE image analysis at 0° using the same procedure than for porosity rate evaluation and is estimated then between 30 % and 40 %. Moreover, the elastic properties of silicon deposited by CVI during SiC deposition are not available to the authors' knowledge. Some studies focus on polycrystalline Si processed by CVD for application in solar panels. In Zibb et al. [35], an elastic modulus of 164 GPa was, for example, measured by nanoindentations. Si was more generally investigated in the case of applications for electronic devices. Thus, Si is manufactured in such a way as to obtain a single crystal by magnification from a melt using the Czochralski or floating zone technique [36], for example. The mechanical characteristics of Si are then largely a function of the crystal orientation of the single crystal. In [36], it varies for example between 100 GPa and 180 GPa at room temperature.

To address this uncertainty, a parametric study was carried out. It allowed to quantify the influence of the quantity of Si and Young's modulus of Si by making the hypothesis that a mixture law with the isotropic characteristics of the SiC matrix and Si allows Si to be incorporated in the core matrix.

Figure 11 shows the modeling error as a function of the amount of Si in the core matrix and Young's modulus of Si. The error is between ±5 % - the same order of magnitude as for the validation on family 1-A - for a Si content between 30 % and 40 % of Si, confirming the in-plane observations on the BSE images. Young's modulus of Si is then between 100 GPa and 140 GPa.

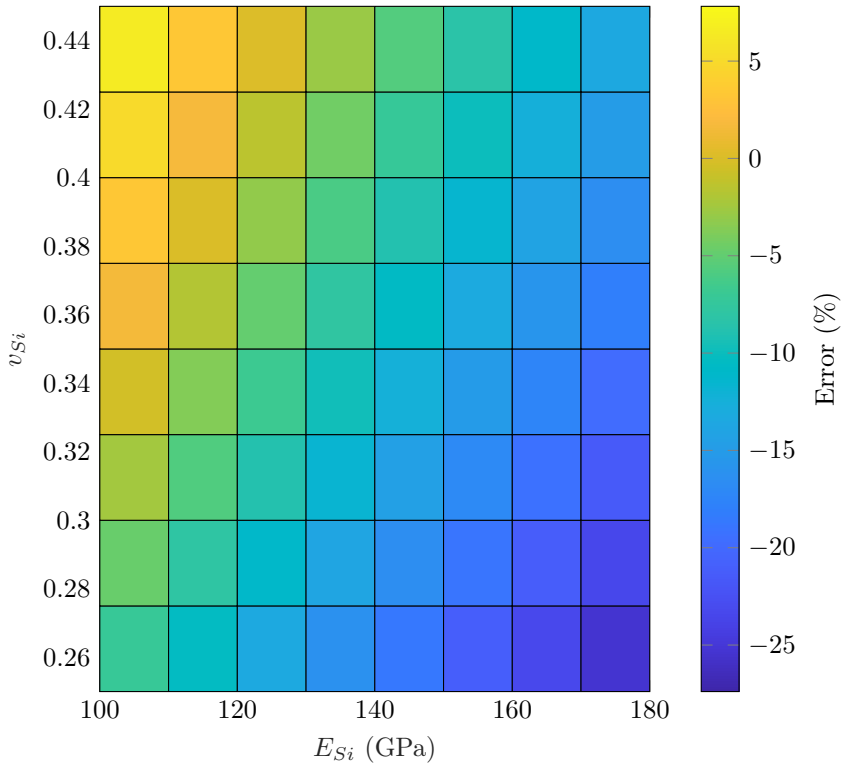

Figure 11: Modeling error for 1-B in function of volumic Si fraction and Young's modulus.

Finally, in the following, the Si fraction is taken to be 35 % in the core matrix and the Si Young's modulus to be 120 GPa. The analytical Young's modulus is calculated to 224 GPa against 212 GPa measured experimentally, with an error of 5 %.

Thus, the core defect of Si in core matrix, ie., the creation and germination of free Si instead of SiC, affect the elastic behavior and leads to a 22 % difference on the elastic modulus between both families 1-A and 1-B.

3.2 Change of regime between elastic and damage domains

The change of regime between elastic domain and the matrix cracking can be defined by two lines on the stress-strain curve. The first line models the elastic behavior, with slope E_e and passing through the coordinate $(0, 0)$. The second line defines the behavior during matrix cracking with a tangent modulus E_{mc}. This line corresponds to the envelope of the strain-stress response without unloading/loading cycles. The tangent modulus during the cracking phase E_{mc} was calculated thanks to two methods for all samples tests as a function of the

test type. If the test was monotonic, the tangent modulus E_{mc} corresponds to the affine regression between 150 MPa and failure. If the test was cyclic, the parts corresponding to the cycles needed to be removed. An affine regression between the end of the second cycle (starting at 150 MPa) and the rupture was performed to obtain the tangent stiffness E_{mc}. The intersection between the two curves - the elastic curve with E_e slope and the damage curve with E_{mc} slope - indicates the deformation at the change of regime between elastic domain and the matrix cracking, labelled ε_{mc}.

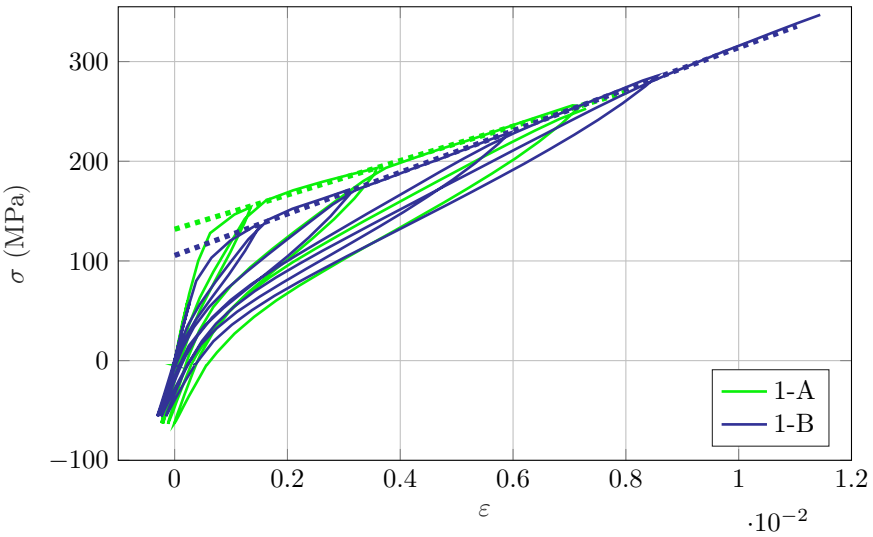

Figure 12: Typical cyclic tensile test for one sample from each family.

It is difficult to determine the influence of Si on the damage mechanisms, since two changes occur between the reference 1-A and the batch 1-B: presence of Si and differences in the seal-coat thickness. The second manufacturing batch allows the separation of the core and the seal coat effect on matrix cracking onset to understand the influence of free Si on the core matrix deformation.

In the second manufacturing batch, i.e., the families 2-RT and 2-WS, the average deformation ε_{mc} of 2-RT was 0.045 % (with a standard deviation of 0.0025 %). In contrast, the average deformation ε_{mc} of 2-WS was 0.063 % (with a standard deviation of 0.0019 %). Thus, by removing the seal coat matrix layers, cracking was delayed by 40 %. The outer matrix on the outside carried out a larger load since it was stiffer than the core of the material. The matrix also exhibits a weaker resistance than the fibers [29]. The matrix behavior that increased load and brittle behavior caused the seal coat layers to crack first.

Figure 13 shows that in the families studying the core defects, 1-A starts to change of domain at a lower strains than 1-B (0.051 % for 1-A with a standard deviation of 0.0011% against 0.063 % for 1-B with a standard deviation of 0.0051 %). The seal-coat matrix between the two families is equivalent (Table 1).

The two layers of the seal coat may not crack for the same strain level. There are several possible explanations for this phenomenon. The seal coat/core interface on the outer surface has a waviness defect in contrast to the inner surface due to the filament winding process, which can lead to a stress gradient. Moreover, the SiC grains deposited by CVI have a specific microstructure consisting of a sizeable columnar arrangement. The SiC matrix present a brittle behavior in particular along the intercolumnar directions of SiC grains [37]. Thus, the grain size increases when the thickness increases, making them more brittle.

The thickness of the outer matrix layer of 1-A is twice that of 1-B. Therefore, the matrix cracking of 1-A starts before 1-B.

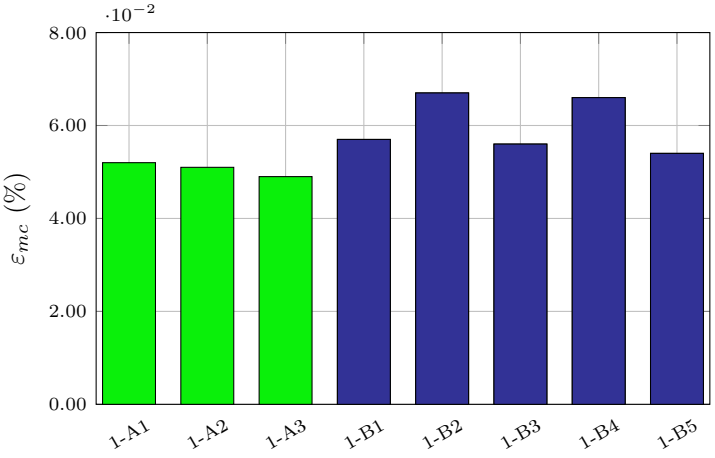

Figure 13: Strain ε_{mc} at the beginning of cracking as a function of the family.

4 Damage mechanisms of SiC/SiC tubes

4.1 Global indicator

In this section, the second part of the stress-strain curve between the matrix cracking start and the ultimate failure was investigated. It was then described by an unique coefficient that refers to the tangent stiffness during the cracking phase E_{mc}. The method to determine this modulus in the case of a monotonic or of a cyclic tensile has been previously described in the Part 3.

The tangent modulus for the two families is given in Figure 14. The two families present 21% of the difference for the modulus E_{mc}: $17.1_{\pm 0.1}$GPa for 1-A versus $21.1_{\pm 0.6}$GPa for 1-B.

Many phenomena occur during cracking, such as load transfer, matrix cracking, slip at the fiber/matrix interface, fiber breakage, etc. The damage appears mainly perpendicular to the loading direction in the case of unidirectional composites, whereas the plies are locally loaded in tension and shear in filament wound tubes. The damage also occurs parallel to the loading direction, resulting

in shear cracks. Studying the envelope alone is difficult in order to understand the damage mechanisms, because of these different phenomena.

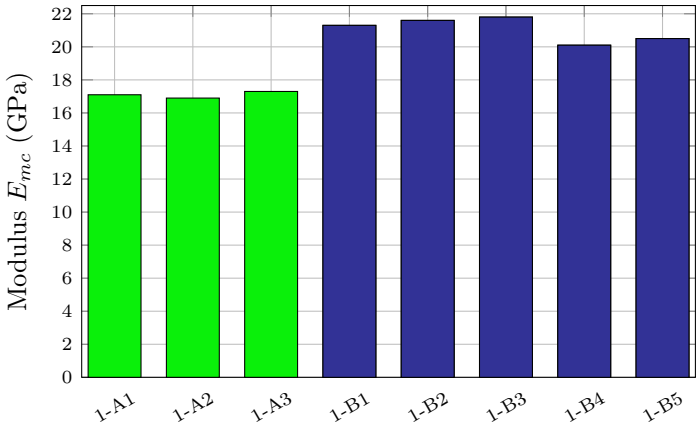

Figure 14: Tangent stiffness during matrix cracking for the two production 1-A (green) and 1-B (blue).

4.2 Analysis of damage behavior on unloading-reloading cycles

The analysis of the envelope of the stress-strain curve does not explain the different damage phenomena in the composite. The cycles can offer additional information to explain these differences. Contemporary behavior models studying the unloading-reloading cycles are carried out at the scale of the plies in the framework of unidirectional materials [27, 28, 38]. The loading is then in the same direction than the fibers. Aveston et al. [39] have studied the influence of the fiber orientation on the cracking direction. The fiber orientation increases loading at the interface. However, the damage mechanisms are similar whatever fiber orientation.

Our analysis of the tubes applies the methodology developed by Domergue and Vagaggini [27, 28] on unidirectional composites, despite the plies local stress in tension-shear (due to the orientation of the plies in the tube axis and the loading). The analysis focuses on the evolution presented in the unidirectional model. No quantitative link on the damage micro-mechanics between the tests carried out in [27] and those shown in the present work are made because of the essential differences between the materials. Particular emphasis is placed on finding coherence between the mechanisms of the unidirectional model and the tube tests.

4.2.1 Description in the unidirectional case

The evolution of the tangent compliance (i.e., inverse of the tangent modulus obtained on the stress-strain curve) during an unloading-reloading cycle can be analyzed in several steps for a unidirectional composite [27, 28]. Figure 15 gives the tangent compliance during an unloading-reloading cycle of a unidirectional composite evolution.

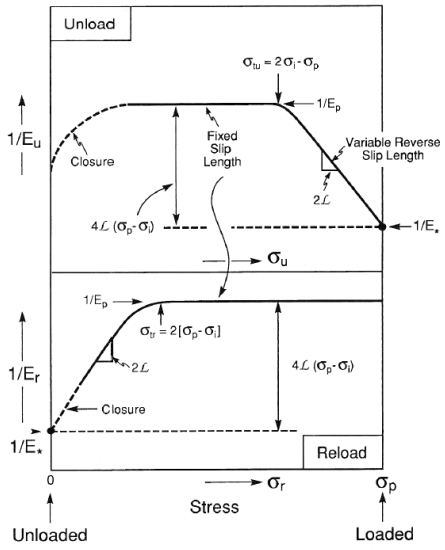

Figure 15: Evolution of the tangent compliance during a unloading-reloading cycle during matrix cracking for a unidirectional composite, extracted from [27].

The shear lag model presents the evolution of the stress in the matrix and the fibers around matrix cracks [26, 30, 40]. The stress in the matrix and the fibers is defined by a law of mixtures far from the matrix cracks. When matrix cracks appear and are deflected at the interface, a load transfer occurs between the matrix and the fibers. Figure 16 presents the stress state around a matrix crack. At the crack opening, there is no stress in the matrix. The load is entirely taken up by the fibers, and a debonding zone appears around the crack. Its length l_d is inversely proportional to the shear stress τ between fibers and matrix. In the debonding zone, the stress in the matrix increases linearly until it reaches the value defined by the law of mixture. During an unloading-reloading cycle, the sign of shear stresses τ changes along the debonding zone.

At the beginning of unloading, fiber and matrix slip at interfaces. The sign of shear stresses τ changes along the debonding zone. The tangent compliance then evolves linearly as a function of the stress until it reaches an asymptote at $1/E_p$, as shown in Figure 15. At the end of the unloading, the cracks close. Reloading starts when $\varepsilon = 0$. The inverse modulus $1/E^\star$ is the tangent compliance at $\varepsilon = 0$ at the end of unloading. In Figure 15, the cycle does not go into

compression, mainly due to residual deformations of thermal origin caused by the manufacturing process. Residual strains then cause the modulus $E^\star$ to be unequal to E_e. Reloading starts with a sliding phase at the fiber/matrix interfaces, exactly at the beginning of the unloading phase, but with the opposite shear stress τ. Just like the unloading, the tangent compliance evolves linearly until it reaches an asymptote at $1/E_p$. The latter remains constant until the end of reloading.

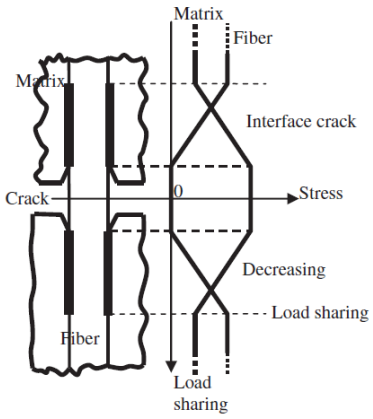

Figure 16: Load transfer between the matrix and a fiber in a unidirectional composite at matrix cracking according to the shear-lag mode [40].

4.2.2 Slipping at fiber/matrix interface

During a cycle, no new cracks are created. The energy loss leading to hysteresis in the unloading/loading cycles comes only from slip. Slipping occurs along the debonding zone around the matrix crack. In the case of more complex structures such as tubes, slipping may also occur at other length scales. For example, plies oriented at $\pm 45^\circ$ can slide at the interface between two strata [15].

Slipping is experimentally characterized by measuring the cycle width at mid-height (i.e., for $\sigma = \sigma_p/2$ with σ_p the stress at the beginning of the unloading cycle) and the cycle area. Regarding the composites studied, 1-A has a higher cycle width than 1-B as depicted in Figure 17. The model only considers the core of the composite and neglects the outer layers effect on the slip. This assumption is consistent with the measurements made on the families 2-RT and 2-WS. The cycle width for these latter families is given in Figure 18. The matrix layers on the outer edges of the tubes have no impact on the slip - only the behavior of the core material plays a role.

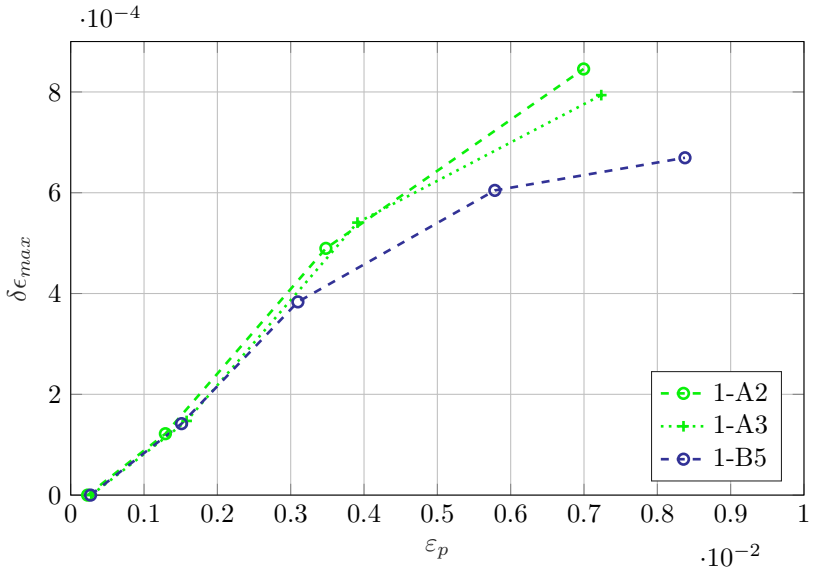

Figure 17: Cycle width at half height for family 1-A and 1-B as a function of deformation.

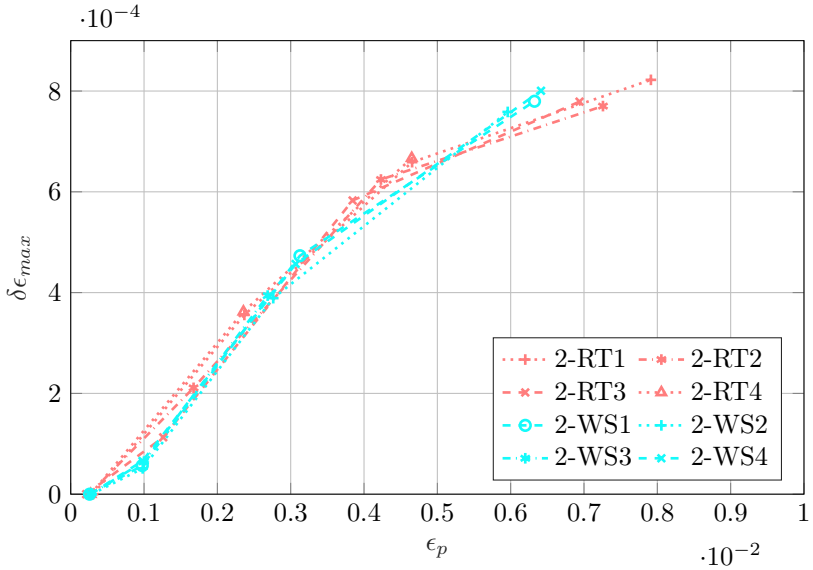

Figure 18: Cycle width at half height for the second batch (2-RT and 2-WS) as a function of deformation.

The composite core is taken at a first approximation as a unidirectional composite. The effect of fiber orientation, likely to result in shear stress, is not

studied here. The macro-scale shear due to fiber orientation is assumed to be identical between all families. In the unidirectional shear lag model, the slip is characterized by the shear stress τ at the fiber/matrix interface. This stress depends on the interphase deposited on the fibers, particularly on its thickness, nature and orientation. The same interphase were probably deposited on each sample, the deposition of the interphase being done simultaneously. So, the shear stress is identical. If so, the differences in behavior observed in Figure 17 cannot be attributed to interphase characteristics.

According to the shear lag model[26], the evolution of stress in the matrix around a crack is defined by

$$\frac{2\tau l_d}{R_f} = \sigma_m(\infty) - \gamma + \sigma_m^T, \tag{1}$$

with τ the shear stress at fiber/matrix interphase, l_d the half-length of decohesion, R_f the fiber radius, $\sigma_m(\infty)$ the matrix stress far away from the cracks, γ the stress equivalent to the energy jump at a matrix crack and σ_m^T the residual thermal stress. Thus, half-length of decohesion l_d is

$$l_d = \frac{R_f}{2\tau}\Big(E_m\varepsilon - \gamma + \sigma_m^T\Big), \tag{2}$$

where the stress away from the crack is equal to $E_m\varepsilon$ with E_m the elastic Young modulus of the matrix. Thus, the greater the elastic modulus of the matrix, the greater is the decohesion length at constant τ. Slipping occurs over a larger area, resulting in a larger cycle width.

Slipping analysis based on the unidirectional model helps to understand the differences observed between the two families. A softer core matrix, such as 1-B, may reduce slip at the interface at constant shear stress τ.

4.2.3 Damage in the loading direction

The evolution of the tangent modulus at the beginning of the unloading is plotted in Figure 19 for the two families 1-A and 1-B. This quantity is characteristic of the damage state in the composite. The slope is determined by linear regression over a stress range between the beginning of the unloading cycle and a stress decreased by 20 MPa. 1-A has a lower tangent modulus $1/E^\star$ than 1-B, between 21 % at the beginning and 17 % at the end of tests.

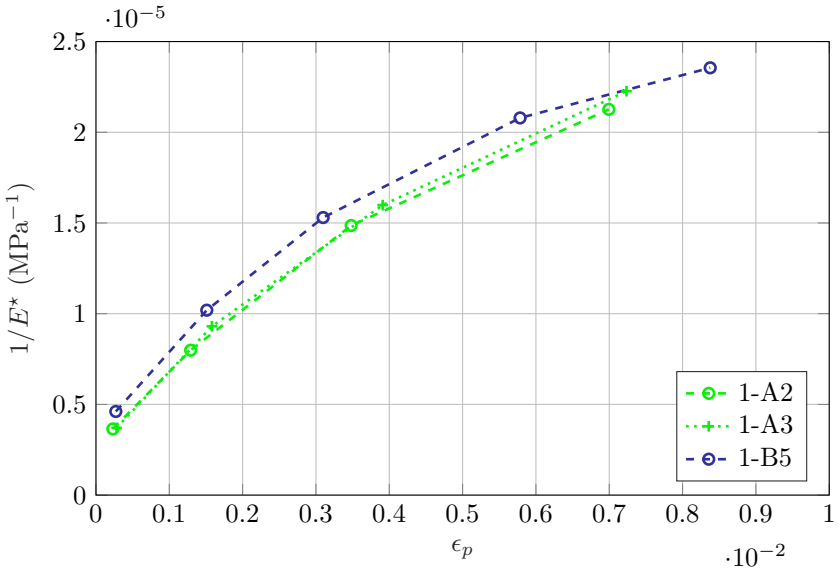

Figure 19: Evolution of the tangent modulus at the beginning of the discharge $1/E^\star$ in function of the strain for 1-A and 1-B samples.

The experimental results on the families 2-RT and 2-WS show that the outer matrix layers have no impact on the evolution of the modulus $1/E^\star$ as shown on Figure 20.

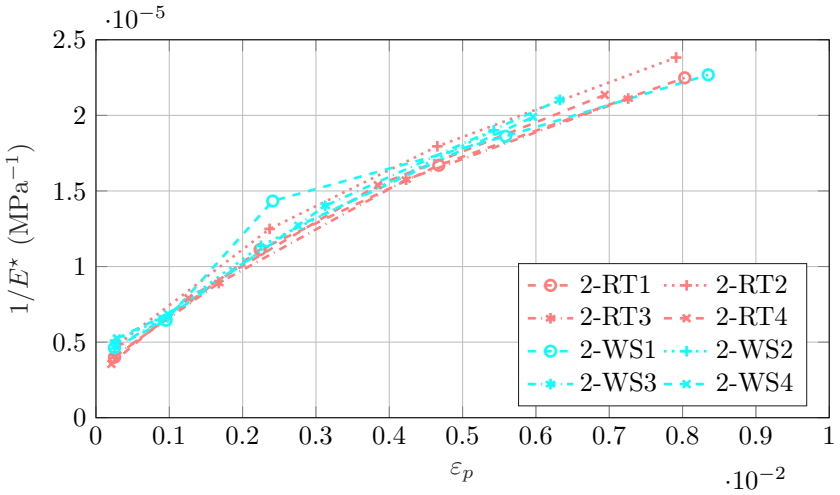

Figure 20: Evolution of the tangent modulus at the beginning of the unloading $1/E^\star$ in function of the strain for families 2-RT and 2-WS.

A quick analysis of the sensitivity of the stiffness loss regarding the one of

the core and the seal coat layers supports this observation. A two-layer material is considered; the first one $\square_c$ corresponding to the core and the other one $\square_e$ corresponding to the outer matrix layers. It is possible to relate the force N applied to the sample to the strain ε from the cross-section $S_\square$, the damage $d_\square$ defined by [41], and the initial elastic modulus $E^0_\square$ of each layer :

$$N = \Big(S_e E^0_e(1-d_e) + S_c E^0_c(1-d_c)\Big)\varepsilon. \tag{3}$$

The average damage is

$$\bar{d} \;=\; 1 - \frac{S_e E^0_e(1-d_e) + S_c E^0_c(1-d_c)}{S_e E^0_e + S_c E^0_c}. \tag{4}$$

By applying a Taylor series of α, then damage $\bar{d}$ is

$$\bar{d} \;\approx\; d_c + \alpha(d_e - d_c) \;\text{ with }\; \alpha = S_e E^0_e / S_c E^0_c. \tag{5}$$

Thus, the average damage of the tubes corresponds to the damage of the core in the first order, followed by the seal coat layers. Furthermore, as seen in the section 3, the outer layers crack first due to their higher stiffness. The outer matrix layer also delaminates, as shown by the red cracks on the postmortem section examination of the specimens of the two families 1-A and 1-B (Figure 21). Therefore, the seal coat certainly has a minimal role in the mechanical behavior of the tubes.

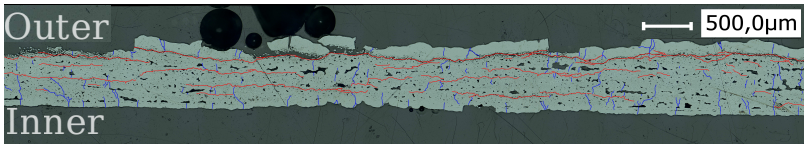

(a) Section from 1-A.

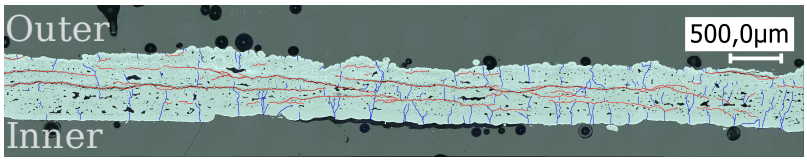

(b) Section from 1-B.

Figure 21: Microscope observations of longitudinal section after ultimate failure for a tube of each families. In blue, the cracks perpendicular to the loading direction and in red the cracks parallel to the loading direction.

A slight difference in the damage behavior in the loading direction was noticed between the families 1-A and 1-B due to the differences measured in the elastic domain ($\approx 20\,\%$). The core composition change was modified similarly to the tangent modulus but did not influence the damage evolution. However, measuring the tangent modulus was complex and is subjected to error. The measurement error is in the order of magnitude of the differences observed in elastic behavior, so it is challenging to conclude further.

4.2.4 Damage in the shear direction

The tangent stiffness at the beginning of reloading $1/E_c$ is measured. In compression, cracks perpendicular to the loading direction are closed. Only cracks loading in shear have an effect on the modulus $1/E_c$. As for the modulus $E^\star$, linear regression is performed on all the measurements comprised between -40 MPa and -20 MPa during the reloading sequence.

Figure 22 shows the evolution of $1/E_c$ as a function of strain for families 1-A and 1-B. A difference in the evolution of the tangent modulus $1/E_c$ is observed. It is not easy to determine if the difference is due to differences in core composition or seal coat thicknesses.

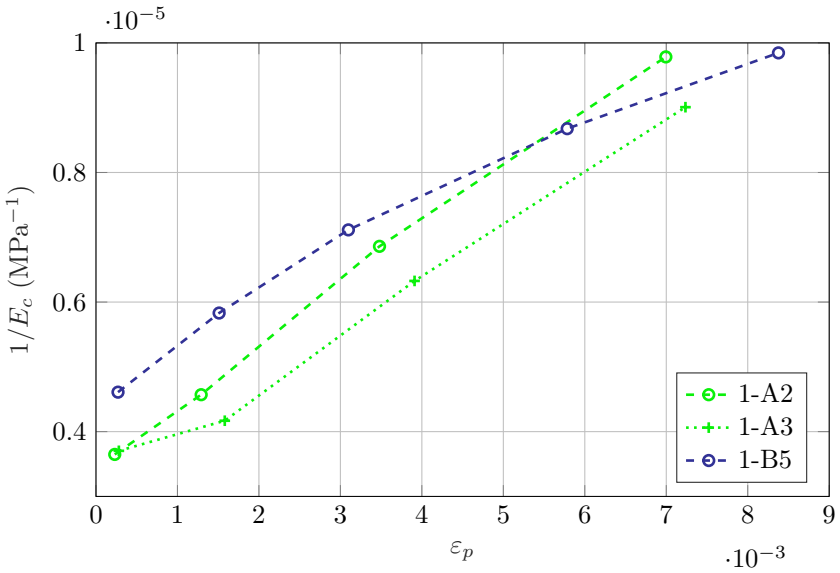

Figure 22: Evolution of the tangent modulus at the beginning of the reloading cycles $1/E^c$ in function of the strain for 1-A and 1-B.

The study of the families 2-RT and 2-WS shows a real influence of the outer layers on shear damage behavior. The outer matrix layer delaminates rapidly and plays a small role in the damage behavior of the tube. On the other hand, the inner matrix layer remains attached to the core. It probably allows recovering part of the load. Thus, the thickness of the internal matrix is greater in 1-B with free Si. It carries a more significant load than in 1-A.

5 Conclusion

Uniaxial cyclic tensile tests provide insight into many of the mechanical phenomena that occur during damage of filament wound SiC/SiC tubular composites.

Tubes 1-B contained free Si in the core ply matrix. This defect significantly changed the monotonic stress-strain curves and led to a decrease in the elastic modulus of the tube. On the other hand, the tangent modulus during matrix cracking and fiber breakage of tubes 1-B was higher than that of reference family 1-A. For the elastic behavior, despite the decrease in porosity for 1-B, due to faster Si deposition kinetics compared to SiC, the presence of Si made the tubes softer. For the behavior during cracking, it is challenging to determine with accurary the influence of the presence of free Si in the core matrix, due to the numerous phenomena involved (matrix cracking, slippage, fiber cracking).

Mechanical characterization of the unloading-reloading cycles was based on model proposed on unidirectional composite [27, 28]. Two variables were particulary considered: the tangent moduli at the beginning of unloading and beginning of reloading, which characterizes of damage, and the cycle width at mid-height $\delta\varepsilon_{max}$, which characterizes fiber/matrix slippage at interfaces. The Si core defects have no influence on the damage in the loading direction, but the second family exhibit slower rate of shear damage and premature saturation of slip at fiber/matrix interface crack.

This experimental study also permitted to highlight the limitations of using an unidirectional model in the case of filament wound tubes. In terms of behavior during cracking, the study of slipping and fracture observations have shown that the unidirectional model is not rich enough to describe the entire behavior of filament wound tubes. This model only considers slipping at the fiber/matrix interfaces with constant shear stress τ, decohesion energy γ, and decohesion length l_d. The model must be enriched to describe the behavior of a tubular composite and include both phenomena highlighted by the experimental analysis. First, the orientation of the fibers and so a local shear loading and the variability of certain parameters must be introduced. Moreover, the load transfer between the seal coat matrix layer and the core must also be considered to predict the shear behavior. Observation in compression highlighted that a part of the cracks were loaded in shear. They slip when they are loaded in compression. This enhanced model would relate microstructure variation and observed mechanical behavior in the presence of core defects.

References

[1] E. Buet, C. Sauder, D. Sornin, S. Poissonnet, J. N. Rouzaud, and C. Vix-Guterl. Influence of surface fibre properties and textural organization of a pyrocarbon interphase on the interfacial shear stress of SiC/SiC minicomposites reinforced with Hi-Nicalon S and Tyranno SA3 fibres. *Journal of the European Ceramic Society*, 34(2):179–188, 2014.

[2] L. Saucedo-Mora, T. Lowe, S. Zhao, P. D. Lee, P. M. Mummery, and T. J. Marrow. In situ observation of mechanical damage within a SiC-SiC ceramic matrix composite. *Journal of Nuclear Materials*, 481:13–23, 2016.

[3] P. Spriet. CMC applications to gas turbines. *Ceramic matrix composites: materials, modeling and technology*, pages 591–608, 2014.

[4] Y. Katoh, K. Ozawa, C. Shih, T. Nozawa, RJ. Shinavski, A. Hasegawa, and L. Snead. Continuous SiC fiber, CVI SiC matrix composites for nuclear applications: Properties and irradiation effects. *Journal of Nuclear Materials*, 448(1-3):448–476, 2014.

[5] Lance L Snead, Yutai Katoh, and Takashi Nozawa. Radiation effects in sic and sic–sic. *Comprehensive Nuclear Materials*, 2020.

[6] KA. Terrani. Accident tolerant fuel cladding development: Promise, status, and challenges. *Journal of Nuclear Materials*, 501:13–30, 2018.

[7] C. Lorrette, T. Guilbert, F. Bourlet, L. Sauder, C. Briottet, H. Palancher, H. Bischoff, and E. Pouillier. Quench behavior of SiC/SiC cladding after a high temperature ramp under steam conditions. In *Water Reactor Fuel Performance Meeting*, Jeju-do, South Korea, 2017.

[8] M. Steinbrueck, M. Grosse, U. Stegmaier, J. Braun, and C. Lorrette. Oxidation of silicon carbide composites for nuclear applications at very high temperatures in steam. *Coatings*, 12(7):875, 2022.

[9] K. Lambrinou, M. Verwerft, J. Vleugels, A. Weisenburger, C. Lorrette, Y. De Carlan, F. Di Fonzo, M. Barzoum, A. Kohyama, and J. Marrow. Innovative accident-tolerant fuel cladding materials the h2020 il trovatore perspective. In *2017 Water Reactor Fuel Performance Meeting*. 2017 Water Reactor Fuel Performance Meeting, 2017.

[10] Nuclear Energy Agency. *State-of-the-art report on light water reactor accident-tolerant fuels*. OECD Publishing, 2018.

[11] Nuclear Energy Agency, Organisation for economic co operation, and development. *CSNI Technical Opinion Papers No. 13 LOCA Criteria Basis and Test Methodology*. OECD Publishing, 2022.

[12] X. Aubard and J. Lamon. Mechanical behaviour of 2 d-woven sic-sic composites under multiaxial loading conditions. In *High Temperature Ceramic Matrix Composites. Proc. 6 th European Conf. on Composite Materials*, volume 20, Bordeaux, France, 1993.

[13] HM. Yun, JA. DiCarlo, and DS. Fox. Issues on fabrication and evaluation of SiC/SiC tubes with various fiber architectures. In *Fifth International Conference on High Temperature Ceramic Matrix Composites (HTCMC-5)*, 2004.

[14] Y. Chen, L. Gelebart, C. Chateau, M. Bornert, A. King, C. Sauder, and P. Aimedieu. Crack initiation and propagation in braided SiC/SiC composite tubes: Effect of braiding angle. *Journal of the European Ceramic Society*, 40(13):4403–4418, 2020.

[15] F. Bernachy-Barbe, L. Gélébart, M. Bornert, J. Crépin, and C. Sauder. Anisotropic damage behavior of SiC/SiC composite tubes: Multiaxial testing and damage characterization. *Composites Part A: Applied Science and Manufacturing*, 76:281–288, 2015.

[16] J. Braun, C. Sauder, J. Lamon, and F. Balbaud-Célérier. Influence of an original manufacturing process on the properties and microstructure of SiC/SiC tubular composites. *Composites Part A: Applied Science and Manufacturing*, 123(October 2018):170–179, 2019.

[17] E. Rohmer. *Caractérisation et modélisation mécanique de tubes composites SiCf/SiC*. PhD thesis, Bordeaux 1, 2013.

[18] E. Rohmer, E. Martin, and C. Lorrette. Mechanical properties of SiC/SiC braided tubes for fuel cladding. *Journal of Nuclear Materials*, 453(1-3):16–21, 2014.

[19] C. Sauder. Ceramic matrix composites: nuclear applications. *Ceramic matrix composites: materials, modeling and technology*, pages 609–646, 2014.

[20] J.F. Maire and D. Pacou. Essais de traction-compression-torsion sur tubes composites céramique-céramique. In *Journées nationales sur les composites*, pages 1225–1234, 1996.

[21] T. Tawakoli and B. Azarhoushang. Intermittent grinding of ceramic matrix composites (CMCs) utilizing a developed segmented wheel. *International Journal of Machine Tools and Manufacture*, 51(2):112–119, 2011.

[22] L. Zhang, C. Ren, C. Ji, Z. Wang, and G. Chen. Effect of fiber orientations on surface grinding process of unidirectional C/SiC composites. *Applied Surface Science*, 366:424–431, 2016.

[23] Q. Liu, G. Huang, X. Xu, C. Fang, and C. Cui. A study on the surface grinding of 2D C/SiC composites. *International Journal of Advanced Manufacturing Technology*, 93(5-8):1595–1603, 2017.

[24] A. Neubrand, J.M. Hausherr, A. Lauer, R. Weiss, and C. Wilhelmi. Investigation of cutting-induced damage in CMC bend bars. *MATEC Web of Conferences*, 29:1–12, 2015.

[25] O. Gavalda Diaz, D. A. Axinte, and D. Novovic. Probabilistic modelling of tool unbalance during cutting of hard-heterogeneous materials: A case study in Ceramic Matrix Composites (CMCs). *Composites Part B: Engineering*, 148(May):217–226, 2018.

[26] N. Lissart and J. Lamon. Damage and failure in ceramic matrix minicomposites: experimental study and model. *Acta Materialia*, 45(3):1025–1044, 1997.

[27] JM. Domergue, E. Vagaggini, and A. Evans. Relationships between hysteresis measurements and the constituent properties of ceramic matrix composites: Ii, experimental studies on unidirectional materials. *Journal of the American Ceramic Society*, 78(10):2721–2731, 1995.

[28] E. Vagaggini, JM. Domergue, and A. Evans. Relationships between hysteresis measurements and the constituent properties of ceramic matrix composites: I, theory. *Journal of the American Ceramic Society*, 78(10):2709–2720, 1995.

[29] C. Chateau, L. Gélébart, M. Bornert, J. Crépin, D. Caldemaison, and C. Sauder. Modeling of damage in unidirectional ceramic matrix composites and multi-scale experimental validation on third generation SiC/SiC minicomposites. *Journal of the Mechanics and Physics of Solids*, 63:298–319, 2014.

[30] JW. Hutchinson and H. Jensen. Models of fiber debonding and pullout in brittle composites with friction. *Mechanics of materials*, 9(2):139–163, 1990.

[31] AG. Evans and FW. Zok. The physics and mechanics of fibre-reinforced brittle matrix composites. *Journal of Materials science*, 29(15):3857–3896, 1994.

[32] C. Sauder and C. Lorrette. Patent EP2683673 (CEA): Method for producing a composite including a ceramic matrix, 2012.

[33] ISO 20323. Fine ceramics (advanced ceramics, advanced technical ceramics) – mechanical properties of ceramic composites at ambient temperature in air atmospheric pressure – determination of tensile properties of tubes. Standard, International Organization for Standardization, 2021.

[34] V. Pensée, D. Kondo, and Dormieux L. Micromechanical analysis of anisotropic damage in brittle materials. *Journal of Engineering Mechanics*, 128(8):889–897, 2002.

[35] MB Zbib, MC Tarun, MG Norton, DF Bahr, R Nair, NX Randall, and EW Osborne. Mechanical properties of polycrystalline silicon solar cell feed stock grown via fluidized bed reactors. *Journal of materials science*, 45(6):1560–1566, 2010.

[36] Akhilesh K Swarnakar, Omer Van der Biest, and Jan Vanhellemont. Determination of the si young's modulus between room and melt temperature using the impulse excitation technique. *physica status solidi (c)*, 11(1):150–155, 2014.

[37] O. Diaz, DA. Axinte, P. Butler-Smith, and D. Novovic. On understanding the microstructure of SiC/SiC ceramic matrix composites (CMCs) after a material removal process. *Materials Science and Engineering: A*, 743:1–11, 2019.

[38] L. Li, X. Guo, and Y. Liu. Characterization of cyclic loading/unloading damage behavior in fiber-reinforced ceramic-matrix composites using inverse tangent modulus. *Journal of the European Ceramic Society*, 42(5):1912–1927, 2022.

[39] J. Aveston and A. Kelly. Theory of multiple fracture of fibrous composites. *Journal of Materials Science*, 8(3):352–362, 1973.

[40] J. Lamon. Approach to microstructure–behavior relationships for ceramic matrix composites reinforced by continuous fibers. *Ceramic Matrix Composites: Materials, Modeling and Technology*, pages 520–547, 2014.

[41] J. Lemaitre and J-L. Chaboche. *Mechanics of solid materials*. Cambridge university press, 1994.